Impact of Glutamate Carboxylation in the Adsorption of the α-1 Domain of Osteocalcin to Hydroxyapatite and Titania

Journal:	*Molecular Systems Design & Engineering*
Manuscript ID	ME-ART-11-2019-000158.R1
Article Type:	Paper
Date Submitted by the Author:	06-Dec-2019
Complete List of Authors:	Alamdari, Sarah; University of Washington, Pfaendtner, Jim; University of Washington, Chemical Engineering

SCHOLARONE™
Manuscripts

In this paper we use molecular simulations to explore if non-specific adsorption of bone proteins onto implant interfaces provides a plausible mechanism of implant fouling, by comparing protein behavior on a model bone surface to a model implant surface. We use enhanced sampling molecular dynamics simulations to model adsorption of the most commonly occurring bone protein, osteocalcin, and its post-translational carboxylation modification onto a crystalline hydroxyapatite and titanium dioxide surface. Here we demonstrate through thermodynamic and structural analysis that the dynamic relationship between a protein and the surface it adsorbs onto is dependent upon differences in solvation, ionization, and post-translational modification. We find that differences in the dominating driving forces at the protein/surface interface give way to changes in adsorption mechanisms. Knowledge about the forces that drive these assemblies on mineral surfaces, and the mechanisms that change these assemblies on titania can be used to augment the design of new implant coatings.

Impact of Glutamate Carboxylation in the Adsorption of the α-1 Domain of Osteocalcin to Hydroxyapatite and Titania

Sarah Alamdari[1], *Jim Pfaendtner[1]

[1]Dept. of Chemical Engineering, University of Washington, Seattle 98195-1750

*Email: jpfaendt@uw.edu

Abstract

One proposed mechanism of implant fouling is attributed to the nonspecific adsorption of non-collagenous bone matrix proteins (NCPs) onto a newly implanted interface. With the goal of capturing the fundamental mechanistic and thermodynamic forces that govern changes in these NCP recognition domains as a function of γ-carboxyglutamic acid (Gla) post-translational modification and surface chemistry, we probe the adsorption process of the most commonly occurring NCP, osteocalcin, onto a mineral and metal oxide surface. Here, we apply two enhanced sampling methods to independently probe the effects of post-translational modification and peptide structure on adsorption. First, well-tempered metadynamics was used to capture the binding of acetyl and N-methylamide capped glutamic acid and Gla single amino acids onto crystalline hydroxyapatite and titania model surfaces at physiological pH. Following this, parallel tempering metadynamics in the well-tempered ensemble (PTMetaD-WTE) was used to study adsorption of the α-1 domain of osteocalcin onto hydroxyapatite and titania. Simulations were performed for the α-1 domain of osteocalcin in both its fully decarboxylated (dOC) and fully carboxylated (OC) form. Our simulations find that increased charge density due to carboxylation results in increased interactions at the interface, and stronger adsorption of the single amino acids to both surfaces. Interestingly, the role of Gla in promoting compact and helical structure in the α-1 domain resulted in disparate binding modes at the two surfaces, which is attributed to differences in interfacial water behavior. Overall, this work provides a benchmark for understanding the mechanisms that drive adsorption of Gla-containing mineralizing proteins onto different surface chemistries.

Introduction

When implants are introduced in the body (e.g. orthopedic or dental), the efficacy of the implanted material is hypothesized to be dependent upon its ability to mineralize or fuse properly with its surrounding tissue.[1–4] This phenomenon, known as osseointegration, takes place at the cell-implant or mineral-implant interface and can be promoted by the chemical or structurally specific design of the implant interface.[5–7] Work in the field of tissue engineering has revealed that specific surface properties of the exposed implant material are influential in guiding these initial cellular events (e.g., protein adsorption to the implant surface) and thus regulating the environment of the extracellular matrix.[4,8,9] In spite of these advances, much remains to be discovered regarding the specific molecular-level recognition mechanisms between bone extracellular matrix proteins (ECM) and both mineral and implant surfaces. This is particularly important for the goal of optimizing the molecular scale design of new materials for implant coatings.

Titanium and its alloys are commonly used as implant materials due to their high biocompatibility and mechanical (load bearing) properties. Upon exposure to oxygen, the highly reactive surface oxidizes and forms a layer of titania (TiO_2) between 2nm and 5nm thick.[10] It has previously been shown that implant treatment with grit-blasting, acid-etching, anodization, or various nanomodification techniques alter the surface roughness and mechanical surface properties resulting in improved osseointegration.[10–14] To further address implant biocompatibility, many groups have looked towards the adhesion of coatings to implanted materials which can improve cell recall to the implant surface.[2,8,15,16] For example, Baranowski et al. demonstrated a bone sialoprotein coating on titania implants first delayed the early stages of osteoblast formation, but ultimately positively influenced ECM mineralization when compared to uncoated titania.[17] Modifications of the implant surface have been shown to impact osseointegration in a variety of ways, which have been extensively summarized by Damiati et al.[18] and Jemat et al.[19] Prior work concludes that the adsorption of cells to the implant surface is highly susceptible to both changes in morphology and chemistry of the surface. However, the fundamental mechanisms driving cell adsorption onto different materials cannot be captured with experiments alone.

The ECM contains both organic and inorganic components. The inorganic component of the ECM is mainly composed of hydroxyapatite (HA) crystals, a calcium phosphate mineral with formula $Ca_5(PO_4)_3(OH)$, and a major component of bone. Osteoblasts are responsible for the production of organic osteoid, which includes both collagen and non-collagenous proteins (NCPs). While collagen makes up approximately 90% of the ECM, NCPs are understood to be key regulators in mineralization.[20–22] NCPs undergo posttranslational modifications (i.e. carboxylation in osteocalcin and matrix Gla protein, or phosphorylation in osteopontin and bone sialoprotein) resulting in an increased negative charge density that has been attributed to the strong adsorption of these proteins onto mineral surfaces.[23] This led to the hypothesis that structurally specific adsorption of NCPs to the newly implanted surface is what allows NCPs to effectively carry out their mineralization role and integrate properly; inhibition of these processes are predicted to promote implant fouling.[5,24,25] Of these NCPs, osteocalcin is the most abundantly occurring and is commonly used as a biomarker in bone health. Its structure is composed of three alpha helical domains with a single disulfide bond between the $\alpha-1$ and $\alpha-2$ domains, and this sequence is highly conserved across porcine, mice, and humans.[26,27] The calcium-binding affinity of osteocalcin is attributed to the presence of 3 vitamin-K dependent post-translationally modified γ-carboxyglutamic acid (Gla) residues located on the $\alpha-1$ domain as shown in Figure 1.

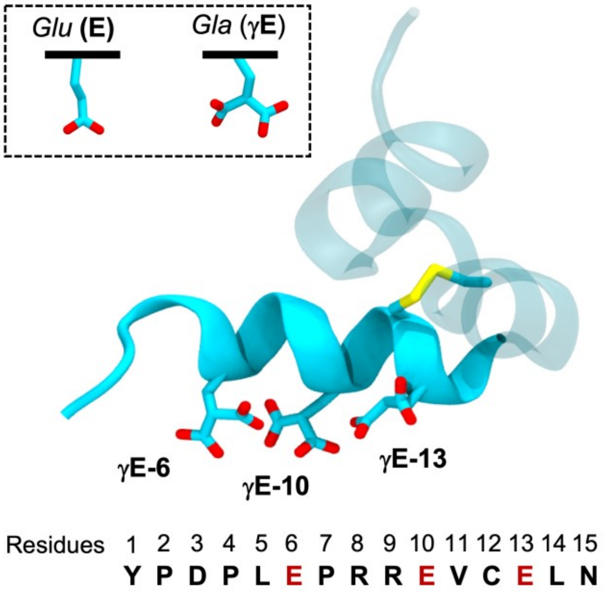

Figure 1. Representation of osteocalcin in its fully carboxylated form (PDB: 1QH8[27]), and the structure of Glu and Gla residues. The α-1 helix containing the first 15 residues is shown in cartoon representation and its sequence is listed below. Other protein residues are presented transparently in cyan. Residues that undergo a posttranslational modification from Glu to Gla are listed in red. Gla residues and residues C23 and C29 between the α–1 and α–2 helices forming a disulfide bond are pictured in licorice and colored by blue carbon, red oxygen, blue nitrogen, and yellow sulfur atoms.

The structure of osteocalcin and decarboxylated osteocalcin in the presence of calcium ions has been studied using circular dichroism, nuclear magnetic resonance (NMR) spectroscopy, and X-ray crystallography in solution concluding the important role calcium ions in producing a secondary structure of the protein in solution.[26–30] Only a handful of studies[31–34] have resolved the structure of biomineralizing proteins on mineral or implant surfaces, and even fewer for NCPs. Notably, in one study Scudeller, et al. used spectroscopy, spectrometry, and isotherm methods to reveal the orientation and conformation of the two forms of osteocalcin on phosphate and silica scaffolds, showing higher adsorption of all forms of osteocalcin on calcium phosphate when compared to silica, and greater helical denaturation on the silica surface.[35] This and another study[30] suggest that the mechanism of mineralization is related to the secondary structure of the adsorbed protein, and is partially dependent upon the surface chemistry of the substrate. To our knowledge there are no experimental studies using these same approaches to probe their structure on titania substrates. Rather, work in this area has focused on macroscopically characterizing osteoblast affinity and function.[36–38] These results, and lack of detail describing the mechanisms that govern these interactions in the literature have inspired additional molecular dynamics (MD) work in this area with the goal of gaining a more microscopic understanding of the behavior of NCPs at mineral and implant interfaces. The role of sequence and post-translational modifications in the biorecognition mechanisms of biomineralizing proteins have previously been studied with success using MD simulations. These studies have been limited in scope, generally focused on understanding the effects of a common post translational modification phosphorylation[39–41], collagen protein[42], and another NCP[43]. Surprisingly, while there is a large interest in understanding phosphorylation, there are few studies that have looked at the effects of Gla post-translational modifications[44,45].

Many prior MD studies on HA have used generalized surface chemistries which corresponded to basic pH.[30,46–48] Older forcefields were modeled after bulk HA crystals lacking parameters for phosphate protonation on the water-exposed surface that occur in biological systems. The lack of parameterization of an interface at realistic conditions was resolved by Lin and Heinz who published a pH specific forcefield in 2016, where changes in pH are accounted for through protonation of surface exposed phosphate groups and the removal of calcium to maintain system charge neutrality.[49] Through this, they demonstrated pH to be influential in peptide adsorption on HA.[49] These limitations in HA simulations have also been discussed extensively by Walsh et al.[50] and continue to be addressed for this complex surface through more robust forcefield development.[44,51–53] Fortunately, this advancement has prompted the ability for new studies to begin to investigate peptide behavior on biologically relevant surfaces. Recently, an enhanced sampling MD study[54] quantified the energetic effects of phosphorylation on the mineralizing protein statherin binding onto HA, and a combined NMR/enhanced sampling MD study[55] uncovered the structure of a statherin mutant on HA, silica, and titania surfaces. These studies motivate using enhanced sampling MD to uncover molecular design rules, a protocol that has shown success in capturing both thermodynamic and structural fingerprints for large peptide-surface systems.

With respect to simulations on titania, there has been a large amount of work in the literature that has simulated the behavior of small molecules and unstructured titania-binding peptides onto titania surfaces[56–59] providing guidance towards understanding the sequence/structure/function relationships of NCPs. Defining the surface of a metal oxide in classical models has proven challenging due to the inability to dynamically represent water dissociation. To tackle this, Předota et al. developed a set of surface models that represent different surface charge states and varying levels surface hydroxylation that describe four plausible molecular-level scenarios occurring at the titania interface in an aqueous environment.[60] With this in mind, we investigated the neutral hydroxylated interface, which allows us to directly probe the influence of surface composition when compared to the neutral hydroxyapatite hydroxylated surface model used in this study. The neutral hydroxylated model provides a model system for the case where the surface of titania is neutralized through the dissociation of water at the interface, forming terminal and bridging hydroxyl groups with exposed titania and oxygen molecules.

The aim of this work was to understand how structure, function, and chemistry of both the surface and peptide manifest in these unique peptide-surface interactions, and ultimately in different biorecognition mechanisms. A deeper understanding of these mechanisms, and the variables that influence them will guide the rational design of new implant coatings. Our approach applied MD simulations and the enhanced sampling method Parallel Tempering Metadynamics in the Well-Tempered Ensemble (PTMetaD-WTE) to extract energetic and structural information of the α-1 domain of carboxylated osteocalcin (OC) and the fully decarboxylated α-1 domain (dOC) adsorbed onto model basal HA (001) and neutral hydroxylated rutile (110) TiO_2 surfaces at physiologically relevant pH. Lastly, we comment on how the results from these simulations can be generalized in the design of new implant coatings.

Methods

The PTMetaD-WTE enhanced sampling method was used for all simulations which has previously been shown to exhaustively sample peptides on surfaces.[61,62] All simulations were performed using GROMACS 2018.3[63] and enhanced sampling simulations were carried out using the Plumed 2.4.2 plugin.[64] The peptides were modeled using the CHARMM36 force field[65] and SPC/E water[66], which are compatible with both of the surface models we implemented. While the CHARMM36 forcefield was designed to be used with TIP3P water model, we chose to use the SPC/E water model which was used in development of the titania model parameters.[60] Previous work understanding the reliability of SPC in combination with CHARMM for biomolecular simulations on titania has shown this is a reasonable choice.[67] Additionally, The INTERFACE forcefield which was parameterized with CHARMM36 in mind, has been shown to capture biomolecular and polymer binding energies within 2-4% using both SPC/E and TIP3P forcefield water models supporting this choice for the HA simulations as well.[68] The Gla forcefield was built by using existing CHARMM36 parameters for glutamic acid, and additional details and parameters used for Gla have been included in the SI. The INTERFACE forcefield[68] was used to model the HA (001) surface, and neutral hydroxylated Rutile (110) TiO2 surface was modeled using parameters from Předota et al.[60], all near pH 7. The pH 10 HA surface given in the INTERFACE forcefield was modified to approximate pH 7 surface by adjusting the ratio of dihydrogen phosphate ($H_2PO_4^-$) and monohydrogen phosphate (HPO_4^{-2}) surface groups to be to be 69%, and 31% respectively (converting 16 dihydrogen phosphate groups to monohydrogen phosphate per face of the surface, 32 total), and adding 8 additional INTERFACE calcium ions per face (16 total). This ratio of phosphate groups is a close approximation of the chemistry at pH 7 (70%/30%). Calcium and chloride counterions were added to neutralize system charge. In recognition of the modified partial charges in the HA model, $Ca^{1.5+}$ ions were used in the HA/INTERFACE system whereas we used the standard Ca^{2+} from the CHARMM36 model for the TiO_2 system to maximize consistency within each model system. Sultan et al. previously verified that the addition of 2+ charge calcium ions can be appropriately used with the negative non-hydroxylated titania surface model, making this an appropriate choice.[69] Table S1 includes information about the system charge and total ions added for each unique simulation.

Each surface was built by replicating the unit cell in the x/y dimension and given a z-dimension of at least 10.5 nm in length to prevent self-interaction across the periodic boundaries. A peptide structure for the α-1 domain sequence shown in Figure 1 was generated in Avogadro 1.2.0[70] and placed near the surface. Following this, the HA surface (7.6 nm × 6.6 nm × 11.0 nm) was solvated with an average of 12,100 water molecules and the TiO_2 surface (5.4 nm × 5.2 nm × 10.7 nm) was solvated with 8,200 water molecules. All systems were first minimized using a steepest descent algorithm to remove any unfavorable contacts over 10,000 steps. A timestep of 2 femtoseconds was used in all simulations, and hydrogen bonds were constrained using the LINCS[71] algorithm. The systems were then equilibrated to standard temperature and pressure, over 1 ns total, using a stochastic global thermostat[72] to couple temperature (tau=0.1 ps) and semi-isotropic pressure scaling using the Parrinello-Rahman barostat[73] (tau=10 ps) with x/y and z compressibility set to 4.5×10^{-15} bar^{-1}, and 4.5×10^{-5} bar^{-1}. Van der Waals interactions were calculated below a cutoff of 1.1 nm, and electrostatic interactions were calculated with particle-mesh Ewald[74] summations using a 1.2 nm cutoff. A 1 ns NVT simulation was then used to generate starting configurations for the enhanced sampling production runs, which were also carried out in the NVT ensemble. During production simulations all phosphate atoms, and all bulk calcium ions in the HA system were held frozen. Similarly, all titanium and all bulk oxygen atoms were held frozen in the TiO_2 system. The bulk atoms are defined to be all the atoms in the surface excluding the first two layers on both the top and bottom interfaces. This was done to preserve surface integrity over the course of the long simulations, while simultaneously allowing interactions with the fluctuating surface atoms.

We first equilibrated 24, and 25 replicas for titania, and HA respectively over 100 ps to temperatures ranging from 300-450K in the NVT ensemble. An ensemble of initial peptide configurations was generated from a 500K NVT simulation of the peptide in water. Different peptide configurations from this trajectory were used as starting structures for each replica. This temperature range has been previously used for biasing large peptides with hidden free energy barriers that are otherwise difficult to sample in the MetaD scheme alone[75]. The specific temperature values for each replica in each system are provided in Table S3. The potential energy was then biased with metadynamics for 10ns, to establish the well-tempered ensemble[76,77] The potential energy was biased using an initial hill height of 2 kJ/mol, a bias factor of 10, and 1hill/1ps hill deposition rate, attempting replica exchange at the same pace. A sigma values of 290 and 400 kJ/mol were used for titania and HA, respectively. These values were calculated by using the half the standard deviation of the smallest equilibrium fluctuations in potential energy from the initial PT simulations, which were all calculated from the lowest temperature replica. The well-tempered ensemble was achieved by observing a constant replica exchange probability near 30% while remaining computationally feasible.[78] In the case of our systems we found 24 replicas were needed with the titania system for 37% exchange probability, and 25 replicas were needed with the HA system for 25% exchange probability. Once WTE was achieved, an additional 2D WTMetaD bias potential was introduced. The WTE deposition rate was reduced by a factor of 5 (1hill/5ps) which has been previously shown to maintain constant exchange, smoothing out any effects from the additional MetaD bias applied to the CVs.[79] This was done to enhance the fluctuations of those slow degrees of freedom to sampling peptide conformation and adsorption on and off the surface. The 2 CVs chosen for this study were; CV1 - peptide radius of gyration using the alpha carbons, and CV2 - the z-distance between the all atom center of mass (COM) of the peptide and a reference surface atom. These CVs were biased using sigma values of 0.2nm, and 0.1nm, respectively, an initial hill height of 2 kJ/mol, a bias factor of 10, and 1hill/1ps hill deposition rate in the 2D MetaD biasing scheme. In this step a harmonic restraint (k = 50,000 kJ/mol/nm^2) was introduced on the z-component of CV2 keeping the peptide within 4.5nm of the surface. This was done to limit sampling to one face of the surface and accelerate convergence. Production runs were extended up until convergence, which is further described in the SI. This window ranged from between 300ns and 500ns per replica for each subsystem. Considering that the total simulation time as the product of simulation time per replica and the number of replicas, this resulted in a total of 6-10 microseconds of computational time needed for each system to reach convergence.

Simulations of acetyl and N-methylamide capped Glu and Gla amino acids were done to characterize the impact of modification alone on adsorption to the surface. Each amino acid was simulated on both surfaces using 4 walkers in the multiple-walker well-tempered MetaD scheme. In the HA system, Ca$^{+1.5}$ INTERFACE ions were used as counterions, in the titania system sodium ions were used as to not introduce any competitive interactions with surface binding as to probe the impact of modification on surface binding energetics alone. Additional system setup details are included in Table S2. Systems were equilibrated using the same criteria as described above. A single 1D bias was added on the z-distance between the COM of all atoms in the peptide analogues.[51] All single amino acid simulations used a sigma value of 0.1nm, initial hill height of 2 kJ/mol, a bias factor of 10, and 1hill/1ps deposition rate. A harmonic restraint (k = 50,000 kJ/mol/nm^2) was introduced on the z-distance to the surface, at 4.5 nm to limit sampling to one face of the surface. These simulations were carried out until convergence, following the same criteria for the other enhanced sampling simulations.

Standard reweighting procedures were used to obtain equilibrium probability distributions for unbiased CVs and is further described in the SI. All corresponding PLUMED input files required to reproduce the results reported in this paper are available on PLUMED-NEST (www.plumed-nest.org), the public repository of the PLUMED consortium (plumID: 19.079).[80]

Results and Discussion

To assess simulation convergence of all enhanced sampling simulations, free energy as a function of the biased CV was monitored over time. Binding free energies were calculated using a Boltzmann averaged difference of the Helmholtz free energy between the surface adsorbed and solution states. All systems were considered converged when the fluctuations in energy were less than k_BT at 300K (~2.5 kJ/mol) for the final 30% of simulation time, during which the system continued to explore CV phase space. The binding free energy time series are included in Figure S1 and discussed in greater depth in the SI.

Influence of Surface Composition

To date and to our knowledge, there are no experimental studies that have reported binding energies of dOC and OC on HA or titania to use as benchmarks for the thermodynamic quantities calculated from simulation. Furthermore, HA and TiO_2 were parameterized with different methods, thus it is important to stress extreme caution should be used in making direct quantitative comparisons between the binding free energies calculated from binding on HA and TiO_2. However, we recently showed in a combined NMR/MD study of statherin adsorption and folding on HA, titania, and silica (using the same forcefields) strong structural agreement between experimental and simulation results, indicating that the surface models are able to sufficiently capture the necessary physics to model these biomolecular-surface interactions.[55]

This study is motivated in estimating the structure of the surface adsorbed peptides and probing the thermodynamic and structural implications of the Gla mutation as a function of changing surface chemistry and charge. We began our investigation profiling the water density for the two surfaces (Figure 2), which match prior reported water densities.[49,60] These water densities are calculated from the nearest frozen heavy atom layer, for each surface respectively. The behavior of water on titania differs fundamentally from that of the hydroxyapatite surface. Most notably, there is a substantial heterogeneous charge distribution in titania resulting in highly ordered water behavior at the interface.[60]. The 001 face of HA, has been characterized as having the least affinity towards water, which is described by a water density profile that contains a peak at a slight distance from the surface.[49]

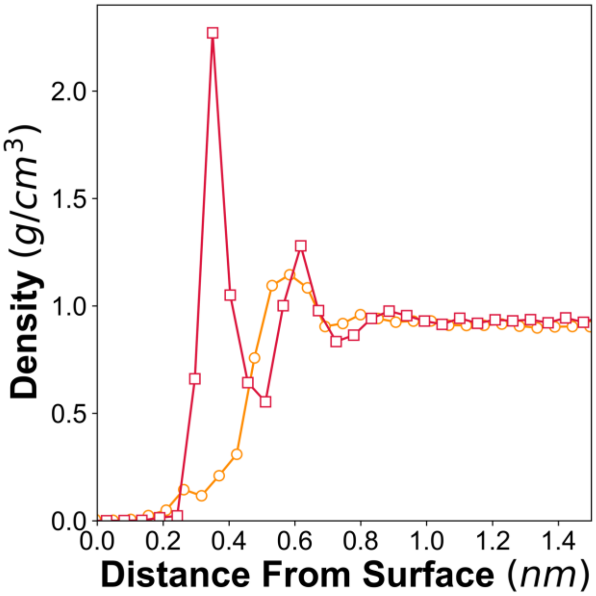

Figure 2. Water density profile on HA (red squares) and titania (orange circles) surfaces.

Similarly, ion affinity varies between the two surfaces. HA contains strong ordered layers of calcium ions within its crystal structure, and a driving force for calcium ions to bind directly to the surface.[49] The behavior of ions on titania has previously been explored by Walsh et. al. on a negative titania surface model where two binding modes were reported; 1) direct surface binding and, 2) water-mediated ion binding.[69] In the case of neutral titania only water-mediated ion binding occurs, and there is no direct affinity observed for the ions to adsorb to the surface, as expected.

Impact of γ-Carboxylation on Glutamate Binding to Surfaces

Binding free energies of capped Glu and Gla amino acids onto each surface were calculated to probe the influence of the modification alone on binding. In Figure 3, Glu and Gla binding profiles on HA were reweighted along the distance between the carboxylate COM and the surface, to gain insight into the minimum energy conformations at the surface. The free energy profiles (FEP) from the biased CVs are included in Figure S2. Gla binds approximately $2k_BT$ stronger than Glu to HA, a direct result of increased electrostatic interactions with the surface, based on the

COM distance to the surface in Figure S2. Interestingly, Glu is able to bind closer than Gla attributed to steric restrictions in the case of Gla, which has a larger sidechain.

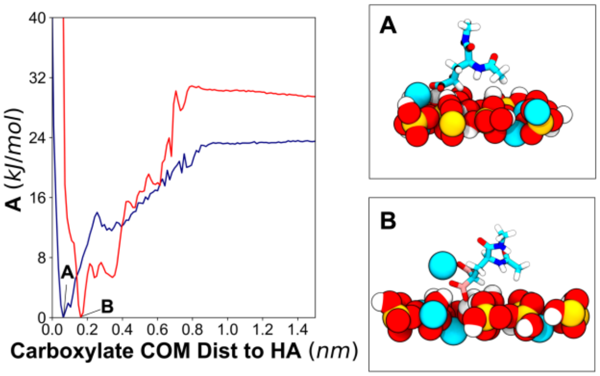

Figure 3. FEP for Glu (blue), and Gla (red) binding onto HA, reweighted along the distance between the carboxylate centers of mass and the surface. Representative structures corresponding to free energy minima are shown for A) Glu and B) Gla, respectively. Surface atoms are colored by orange phosphorous, red oxygen, white hydrogen, and cyan calcium. Amino acids are shown in licorice representation, corresponding to the same color scheme as Figure 1.

The TiO_2 binding profile in Figure 4 contains many more features than HA, indicating adsorption behavior on the two surfaces is influenced by fundamental differences in the surface chemistry. Similar to HA, both Glu and Gla were found to bind to TiO_2 through direct sidechain interactions with surface atoms. In HA, this was largely attributed to interactions with calcium, in TiO_2 binding is achieved with surface hydroxyl groups. Gla binds approximately $5k_BT$ stronger than Glu to the surface, based on COM binding energies reported in Figure S1 which is also directly attributed to increased surface interactions. Similar to HA, Glu was able to bind much closer to the surface than Gla, likely due to steric reasons exemplified in Figures 4A and 4D, which represent then minimum energy structures bound closest to the surface. Interestingly, the strongly adsorbed water layer formed on titania was able to support water-mediated binding poses (Figure 4C and 4F) with a considerable binding affinity in the case of both Glu and Gla.

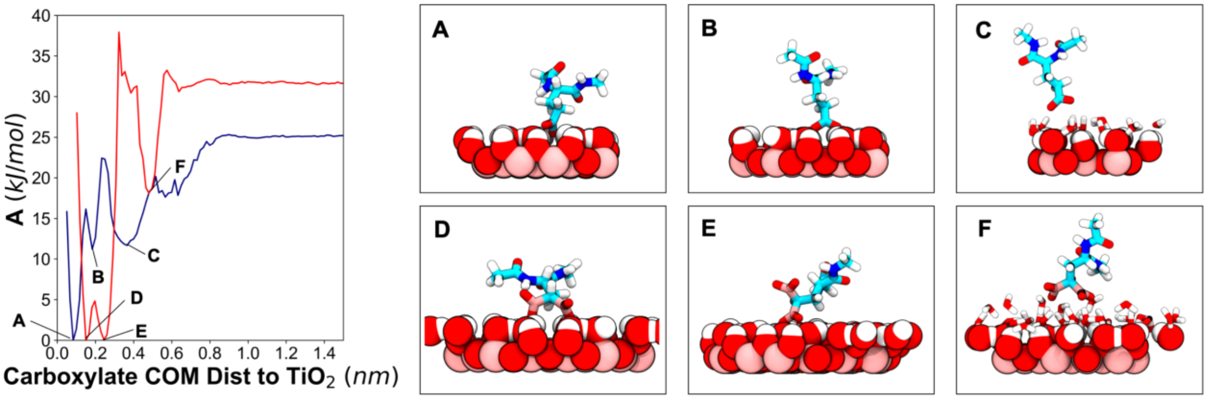

Figure 4. FEP for Glu (blue) and Gla (red) binding to TiO_2 reweighted along the distance between the carboxylate centers of mass and the surface. Representative structures for free energy minima associated with Glu binding are shown in (A), (B) and (C). Minima structures for Gla binding are shown in (D), (E), and (F), and labeled on the FEP. Surface atoms are shown in pink for titania, red for oxygen, and white for hydrogen.

The single amino acid binding profiles reveal site-specific adsorption to HA and TiO_2 for both wild type glutamate as well its carboxylated version. The presence of positively charged sites on both surfaces, with a favorable register against the spacing of negative charges on the amino acid sidechains leads to increased binding for the Gla residue in approximately the same amount on both surfaces. However, the contributing factors to binding are not solely due to the increased Coulombic interactions from the side chain owing to the fact that both HA and TiO_2 show roughly a 1/3 increase in binding energy upon carboxylation. Thus, other factors such as van der Waals interactions or Coulombic interactions from the backbone may also substantially contribute to binding.

Glutamate Carboxylation Influences Peptide Binding Affinity through Interfacial Structure

To explore the impact of modification on the magnitude of binding to HA and TiO_2 binding affinities for both systems were calculated for the fully unmodified (dOC – containing all Glu residues) and fully modified (OC – containing all Gla residues) forms of the α-1 helix and shown in Figure 5 (n.b., here we follow consistent nomenclature from the literature adopting dOC and OC in discussing osteocalcin posttranslational modifications). In the case of HA, OC binds with over twice the affinity, and slightly closer to the surface than dOC. The OC sequence is more negatively charged than dOC, indicating adsorption to HA is driven by electrostatic interactions, and subsequently the overall charge density of the system agreeing with what was predicted from the single amino acid binding profiles. Electrostatic driven binding has also been reported for phosphorylated peptides to metal oxide surfaces[81], LK peptides on negative self-assembled monolayers[79], and large globular proteins lysozyme and α-lactalbumin at charged interfaces[82]. In contrast, on the titania surface there was almost a tenfold decrease in the binding affinity with increasing charge density; dOC bound much stronger to the surface than OC, and OC was also bound much further to the surface than dOC. These non-linear binding trends prompted further exploration into the role of peptide structure on the impact of binding.

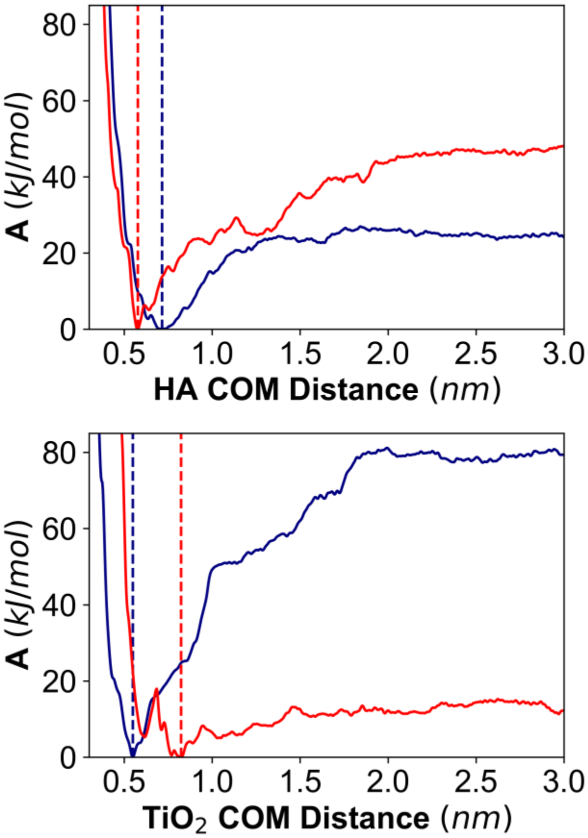

Figure 5. FEP for dOC (blue) and OC (red) for the all-atom peptide COM distance to HA (top) and TiO_2 (bottom). Dashed lines indicate location of free energy minima on each FEP.

Structure, configurational entropy, and the behavior of water on the two surfaces are discussed as dominating driving forces causing differences in adsorption behavior. Free energy surfaces (FES) describing the peptide distance to the surface, and radius of gyration were used to characterize surface-bound and solution peptide structure of each system. The radius of gyration was reweighted based on solution (distance > 3.0 nm) and surface (distance <= 3.0) distance from the surface, to clearly understand the impact of modification on structure. The 2D FES are provided in Figure S9 for reference. Clustering techniques were then used to describe the peptide structure at minimum energy regions on the FES and to further quantify entropic driving forces. And lastly, reweighted FES were used to quantify contacts between the peptide modification sites and the surface which are further discussed in detail in the SI.

Figure 6 shows the structural analysis for the surface bound states of dOC and OC adsorbed to HA (i.e. a COM distance <= 3.0 nm). The free-energy profile for the peptide radius of gyration shows that dOC adopts an extended conformation at the interface, given by the free energy minima at a radius of gyration value of 1.2 nm. This extended conformation persisted in all 3 of the top structures from clustering the structures at the surface, representing over 50% of the surface bound conformations (Figure S3). A similar analysis for configurational energy was done for the peptide in solution (i.e. at COM distances > 3.0 nm from the surface) and is given in Figure S5, with the top structures from clustering given in S7. In solution, dOC adopts a slightly extended conformation, but the energetic differences between collapsed and extended states are significantly smaller than the adsorbed state, indicating the unmodified peptide has no conformational preference in solution.

In contrast, the carboxylated peptide OC shows a stabilized collapsed or compact structure on the surface. Additionally, OC demonstrated helical adsorption onto HA, which persists in the top clusters (Figure S4). This helical structure captured in Figure 6B and C, is slightly different from the helical structure proposed by the solution studies in Figure 1 where helices are presumed to be stabilized due to strong Gla/divalent interactions in solution. In the surface adsorbed structure of OC, a kinked tight helix with two turns appears in two of the top clusters, representing 79% of all adsorbed conformations. This kinked helix was found to be due to strong stabilized amino acid/ion interactions between Asp-3 and Gla-6 and the surface, and a proline residue (Pro-5) induced kink in the backbone. Two different hydrogen-bonding modes forming an irregular helix were found to occur in the backbone and have been characterized further in Figure S12. No helical structure is observed past residue Arg-9, in the second half of the peptide. In the full osteocalcin sequence, a disulfide bond at position 12 acts as a stabilizing bridge between the α-1 and α-2 domains, suggesting the presence of the second helical domain might be critical in stabilizing structure in the second half of the α-1 domain. Scudeller et. al. proposed that the α-2 domain also adsorbed onto HA, prompting future investigation in the role of this second domain and its stabilizing disulfide bond.[35] Unlike dOC, OC takes on a distinctly more compact form in solution (Figure S5 and S8). This indicates that the combination of calcium and carboxylation lead to a distinct solution structure. This agrees with previous experimental work which has reported OC to be unstructured in solution without the presence of Ca^{2+} ions, and supports the importance of the Gla modification in promoting structure of the full protein.[83]

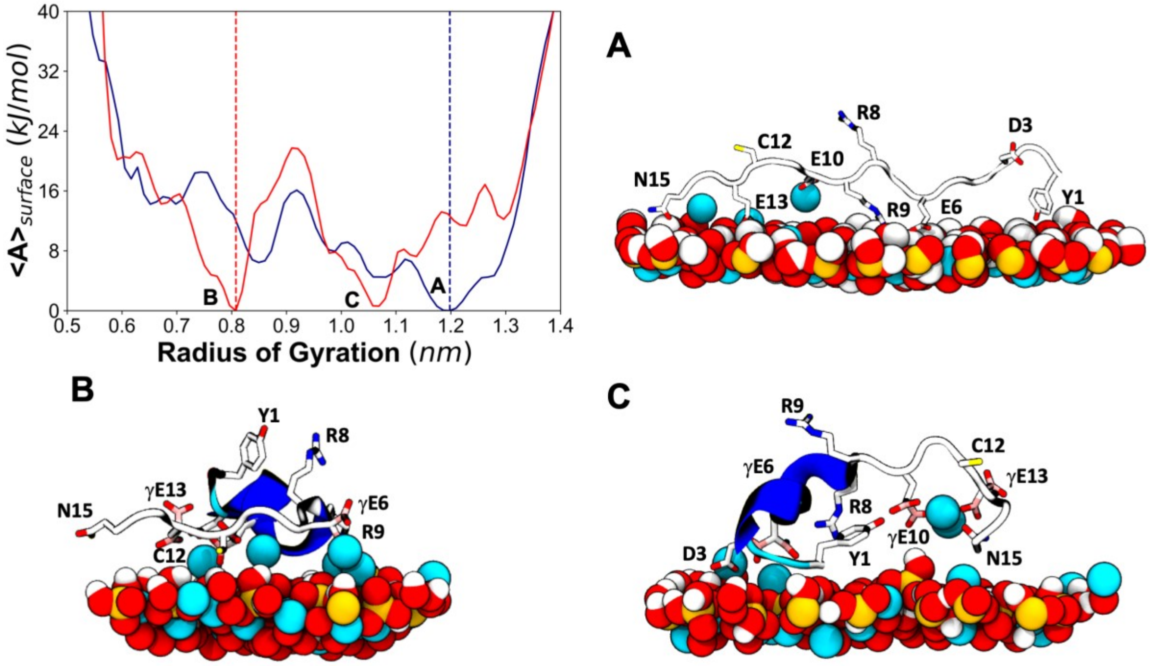

Figure 6. Reweighted 1D FEP for dOC (blue) and OC (red) adsorbed on HA along the radius of gyration calculated from c-alpha atoms. (A) Representative snapshot of the lowest free energy minima found for dOC, representing 38% of the surface adsorbed structures. Representative snapshots of the free energy minima for OC at positions B) and C) on the FES. OC structures represent the ensemble of configurations described by cluster 1 and 2 (Figure S4) which in total accounts for 79% of the surface adsorbed structures. Amino acids are labeled and represented in licorice, not including hydrogens, carbons are shown in white. Nonpolar non-interacting amino acids were omitted from the representation for clarity. The structure of the peptide is represented by the new cartoon drawing scheme colored by structure, where a 1-4 helix is shown in purple, irregular helices are given in royal blue, turns are represented by cyan, and coils are shown in white.

To further characterize increased binding due to increased interactions at the surface, the simulations were reweighted to quantify the number of interactions between Glu or Gla residues and the surface. The reweighted FES for dOC on HA shows that the adsorbed peptide has an average of 1 O-H interaction, and 2 O-Ca^{1+5} interactions with Glu (Figure S10) indicating the extended surface adsorption is a function of many residues on dOC interacting with the surface. As shown in Figure S10, OC adopts a number of energetic minima at the surface. The deepest free energy minima accounts for an average of 6 O-H interactions, and 13 O-Ca^{1+5} interactions with Gla. In this case, carboxylate side groups are stabilized by both protein/surface and protein/ion interactions. The modification resulted in a larger binding free energy, which can directly be described through increased surface contacts, and closer binding to the surface. This indicates enthalpic contributions act as a dominant driving force in HA-adsorption.

As noted above, the adsorption thermodynamics on neutral TiO_2 were found to be dramatically different compared to HA for both peptides. The unmodified peptide (dOC) was shown to have a much larger binding affinity towards the surface than the carboxylated form (OC), opposite the single amino acid predictions. This indicates the role of structure is a critical consideration in these systems. Interestingly, although demonstrating different binding affinities, the both HA and TiO_2 showed similar structural behavior at the interface and in solution. As shown in Figure 7 dOC is extended at the surface, and this persists in all of the top clusters, as shown in Figure S3. This mechanism of interaction is similar to a recent study showing that extended phosphorylated R5 peptides derived from silaffin strongly bind quartz surfaces compared to collapsed and more globular peptides.[39] Similarly, OC adopts a compact form at the surface, with some structure in the top clusters shown in Figure S8. A similar kinked helix as described in Figure S12, is seen in the top structures for TiO_2, but less prominently than upon adsorption to HA. This is attributed to differences in the crystalline structure of the two surfaces, which do not contain bound calcium ions, and the alternate modes by which the peptide interacts with the surface.

It is important to note that while we can predict that the $Ca^{1.5+}$ interactions could be underestimating the energetic impact on structure especially in solution, we see the same conformational trends in solution (albeit to a lesser degree in the case of the $Ca^{1.5+}$ containing system) independent of the charge on calcium used; dOC shows little structural preference in solution whereas OC adopts a significantly compact conformation in solution (Figure S6). Future work should look to investigate the impact of the HA force field's use of $Ca^{1.5+}$ and the energetic impacts on GLU and GLA binding, perhaps with the use of DFT simulations to accurately capture solvation free-energies and enthalpic contributions to the binding free-energy.

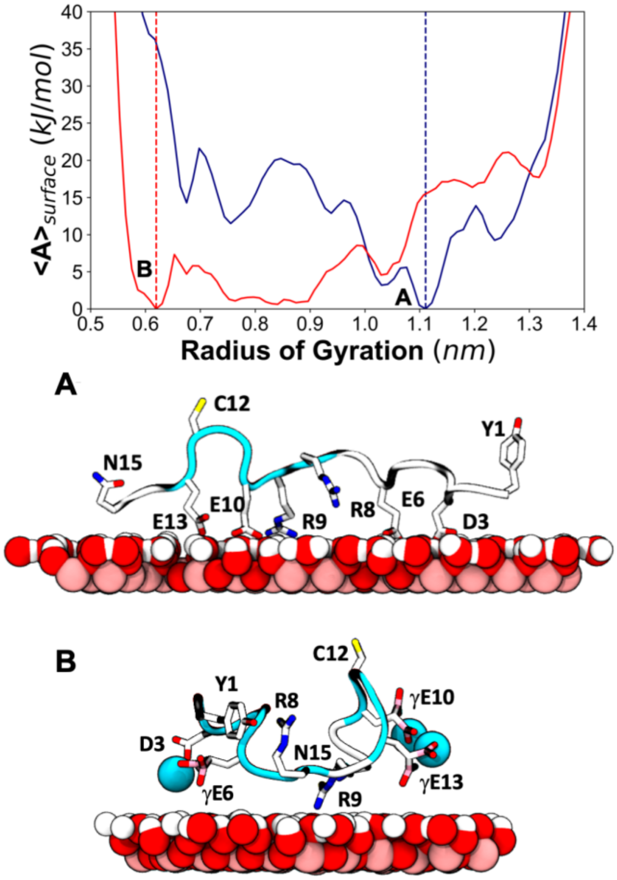

Figure 7. Reweighted 1D FEP for dOC (blue) and OC (red) on TiO_2 along the radius of gyration calculated from c-alpha atoms. (A) Representative snapshot of the lowest free energy minima found for dOC, representing 41% of the surface adsorbed structures. Representative snapshots of the free energy minima for OC at positions B) representing 21% of the surface adsorbed structures. Follows coloring scheme from Figures 4 and 6.

The FES for dOC shown in Figure S11, demonstrates that the Glu residues are highly coordinated with hydroxyl groups on the titania surface with an average of 7 O-H interactions, and 3 O-Ca^{2+} interactions. In contrast, the minimum energy OC adsorbed structure has no O-H Gla interactions (no interactions with the surface), and highly interacts with calcium over an average of 8.5 O-Ca^{2+} Gla interactions. This indicates that the negative modified Gla residues strongly prefer to coordinate with calcium over the surface hydroxyls. In the neutral surface, there is no electrostatic driving force for positive calcium ions to adsorb directly to the neutral surface. The surface bound structure is instead stabilized by few water-mediated interactions of both the ions and arginine residues, giving rise to weakly bound interactions. This minimum energy binding pose, and high affinity to interact with calcium, explains the over tenfold reduction in binding energy that was reported in Figure 5. Similar solvent-mediate contact has been reported in titania binding peptides, when calcium ions were introduced to the system.[69] Peptide/calcium affinities compete with direct peptide/surface binding in the case where there are no ion/surface driven interactions.

Configurational Entropy

To further understand the trends in binding across the different surface chemistries we used a configurational entropy analysis on the peptide structures. A clustering analysis on surface and solution phase structures was used to assess the probability of each of the microstates (p_i). The change in conformational entropy upon adsorption ($\Delta S_{ads,config}$) was obtained by difference between the solution ($S_{sol,config}$) and absorbed states ($S_{surf,config}$) using Equations 4-5.

$$TS_{config} = -k_B T \sum_{0}^{i} p_i \ln(p_i) \tag{4}$$

$$T\Delta S_{ads,config} = TS_{surf,config} - TS_{sol,config} \tag{5}$$

Convergence of this analysis is demonstrated in Figure S13. This method has previously been used to estimate LK-peptides adsorbed onto SAMs[79] and does not include translational or rotational degrees of freedom, which are assumed to be less significant in this case. The entropy calculations are given in Table 1. All systems, except the adsorption of OC onto neutral titania demonstrate an entropic penalty upon adsorption with the solution phase showing more conformational flexibility. As noted in Table S2, each system contains a unique number of ions due to the protocol of charge neutralization that was used for setting up each simulation. Therefore, great care should be taken in comparison between the different solution phase entropy values only, although the *ΔS* values should be comparable across all systems.

Table 1. Change in configurational entropy at 300K

Surface	*Peptide*	$TS_{surf,\,config}$ (kJ/mol)	$TS_{sol,\,config}$ (kJ/mol)	$T\Delta S_{ads,\,config}$ (kJ/mol)
HA	dOC	1.48	6.37	-4.88
HA	OC	0.91	3.17	-2.26
TiO_2	dOC	0.69	5.09	-4.41
TiO_2	OC	2.50	1.19	+1.31

A larger entropic penalty was found for dOC adsorption onto HA, and for dOC adsorption onto TiO_2. As described above, both peptides adsorb in a similar, extended and rigid confirmation. OC adsorption experienced less of an entropic penalty, compared to dOC in both systems. In addition to configurational entropy, previous work on peptide adsorption[50,56,79] report that the entropic gains from tightly bound water layers can often be used to explain the driving forces behind peptide binding affinities on metal oxides and strongly hydrophobic surfaces. And similarly, large binding affinities have also been reported for extended peptides binding onto other surfaces.[39] As noted above although care should be taken when comparing energetics across different force fields, we expect the entropic gains due to water when the peptide binds on TiO_2 to be much larger than when binding on HA from the water density profiles given in Figure 2. This can partially rationalize the large difference in binding free energetics between two structurally similar systems, which experience different driving forces.

In contrast to dOC, binding of OC shows different entropic trends between the two surfaces. While they were structurally similar, binding on HA was mediated by ion interactions at the surface, and binding on TiO_2 was driven by water-mediated binding of ions and the peptide sidechains. Calcium ions have previously been shown to influence the structure of titania binding peptides thereby influencing conformational flexibility when adsorbed on titania.[56,69] The increase of binding entropy on OC adsorption to TiO2 is consistent with the other energetic and structural analyses, namely that this peptide binds the weakest (Figure 5) and furthest from the surface (in a water-stabilized binding mode) and shows a wide range of stable Rg values on the surface (Figure 7).

Conclusions

This paper presents a comprehensive study of the behavior of the first domain of Osteocalcin interacting with different model surfaces. Using single amino acid studies as a starting point, we described the effect of a common Gla post-translational modification on binding to the two surfaces. In both systems, the modification increased overall binding to the surface, however we observe disparities in the binding mechanisms which can be attributed to differences in the behavior of water and ions on each surface. A strongly adsorbed water layer on TiO_2 promotes competitive binding modes that can occur at the surface. To further explore the impact of glutamate carboxylation on structure and energetics, we used enhanced sampling to capture the behavior of the α-1 helix on both surfaces.

Simulations showed that the Gla-modification provides stable binding with surface adsorbed calcium ions, giving way to helical structure. These peptide/surface interactions result in uniquely kinked helix that occurs in the first 7 residues due to strong interactions between aspartic acid, Glu, and Gla with surface ions and the presence of prolines in the peptide backbone. We predict that a fully helical structure of α-1, which was not captured in these simulations, may be partially dependent on adsorption and stability of the α-2 helix, which was also previously predicted to bind to HA experimentally.[35] A single disulfide bond between the α-1 and α-2 helices would provide a significant amount of stability to the N-termini that was seen to be flexible and random coil in all simulations, prompting further investigation by simulation into more complex systems.

dOC was found to behave similarly on HA and TiO_2, adsorbing in an extended and unstructured conformation. Differences in binding affinities of the similar structures, while not definitive, are likely explained by the differences in water behavior on the two surfaces, and differences in competing interactions at the interface (i.e. entropic over enthalpic binding affinities). Gla induced structure in the case of OC, resulted in further differences in the binding modes on the two surfaces. Gla was able to promote both structure and binding on HA, due to calcium ions bound to the HA surface. Alternatively, while Gla promoted structure in the case of TiO_2, a lack of ions bound directly at the titania interface gave rise to enthalpically driven solvent-mediated binding of structured OC on TiO_2.

Osteocalcin adsorption appears to not only be a function of the specific protein/surface interactions as a function of post translational modifications but is highly dependent upon the behavior of water and ions surrounding the surface. This environment surrounding titania resulted in mechanistically different adsorption when compared to HA. Increased peptide/ion interactions appear to be important in eliciting helical structure, which are stabilized by the post translational carboxylation modification, and was found to be a dominating driving force, enhancing peptide adsorption to HA, and disrupting binding to TiO_2.

Our study helps suggest design principles for surface coatings that could help promote binding similar to the natural HA surface. Namely, design of implant coatings should consider two aspects found to be critical in replicating adsorption to HA; 1) high enthalpic (electrostatic) driving must be designed into the system (i.e. some inherent affinity of the surface for calcium), and 2) surfaces should minimize strong ordering of water. Effects like surface etching and modification that disrupt the highly crystalline nature of a titania surface and improve osseointegration may indirectly impact the effect of tightly bound waters at the surface, prompting further consideration and investigation from both an experimental and simulation standpoint. Similarly, the use of negative or non-hydroxylated surface titania surfaces could positively influence more direct calcium-surface interactions, prompting further investigation into additional model simulations.

Nonetheless, the ability to gain some insight into the driving forces of these protein-surface interactions using simulations alone is exciting. These simulations are a first look at understanding the mechanisms that govern protein binding interactions at mineral and implant surfaces in the ECM and prompt future studies.

Acknowledgements

This material is based upon work supported by the National Science Foundation Graduate Research Fellowship Program under Grant No. DGE-1762114 and in part by National Institute of Health award R21-A126113. Part of the simulations in this work were facilitated though the use of advanced computational, storage, and networking infrastructure provided by the Hyak supercomputer system and funded by the STF at the University of Washington. The authors would like to thank Rachel Gebhart, Gary Drobny, Janani Sampath, and Orion Dollar for their helpful discussions and insight.

References

1 K. Anselme, *Biomaterials*, 2000, **21**, 667–681.
2 J. Raphel, M. Holodniy, S. B. Goodman and S. C. Heilshorn, *Biomaterials*, 2016, **84**, 301–314.
3 M. Sundfeldt, L. V. Carlsson, C. B. Johansson, P. Thomsen and C. Gretzer, *Acta Orthop.*, 2006, **77**, 177–197.
4 D. A. Puleo and A. Nanci, *Biomaterials*, 1999, **20**, 2311–2321.
5 A. F. Mavrogenis, R. Dimitiou and G. C. Babis, *J. Musculoskelet. Neuronal Interact.*, 2009, **9**, 61–71.
6 K. Anselme, M. Bigerelle, B. Noël, A. Iost and P. Hardouin, *J. Biomed. Mater. Res.*, 2002, **60**, 529–540.
7 F. Marco, F. Milena, G. Gianluca and O. Vittoria, *Micron*, 2005, **36**, 630–644.
8 B. D. Bovan, T. W. Hummert, D. D. Dean and Z. Schwartz, *Biomaterials*, 1996, **17**, 137–146.
9 W. Orapiriyakul, P. S. Young, L. Damiati and P. M. Tsimbouri, *J. Tissue Eng.*, 2018, **9**, 204173141878983.
10 M. Nair and E. Elizabeth, *J. Nanosci. Nanotechnol.*, 2015, **15**, 939–955.
11 H. J. Rønold, S. P. Lyngstadaas and J. E. Ellingsen, *J. Biomed. Mater. Res. Part A*, 2003, **67A**, 524–530.
12 O. Omar, D. Karazisis, A. Ballo, S. Petronis, H. Agheli, L. Emanuelsson and P. Thomsen, *Int. J. Nanomedicine*, 2016, 1367.
13 V. Goriainov, G. Hulsart-Billstrom, T. Sjostrom, D. G. Dunlop, B. Su and R. O. C. Oreffo, *Front. Bioeng. Biotechnol.*, 2018, **6**, 1–14.
14 L. Salou, A. Hoornaert, G. Louarn and P. Layrolle, *Acta Biomater.*, 2015, **11**, 494–502.
15 R. P. van Hove, I. N. Sierevelt, B. J. van Royen and P. A. Nolte, *Biomed Res. Int.*, 2015, **2015**, 1–9.
16 Z. S. Tao, W. S. Zhou, X. W. He, W. Liu, B. L. Bai, Q. Zhou, Z. L. Huang, K. K. Tu, H. Li, T. Sun, Y. X. Lv, W. Cui and L. Yang, *Mater. Sci. Eng. C*, 2016, **62**, 226–232.
17 A. Baranowski, A. Klein, U. Ritz, A. Ackermann, J. Anthonissen, K. B. Kaufmann, C. Brendel, H. Götz, P. M. Rommens and A. Hofmann, *PLoS One*, 2016, **11**, 1–23.
18 L. Damiati, M. G. Eales, A. H. Nobbs, B. Su, P. M. Tsimbouri, M. Salmeron-Sanchez and M. J. Dalby, *J. Tissue Eng.*, 2018, **9**, 204173141879069.
19 A. Jemat, M. J. Ghazali, M. Razali and Y. Otsuka, *Biomed Res. Int.*, 2015, **2015**, 1–11.
20 P. Ducy, C. Desbois, B. Boyce, G. Pinero, B. Story, C. Dunstan, E. Smith, J. Bonadio, S. Goldstein, C. Gundberg, A. Bradley and G. Karsenty, *Nature*, 1996, **382**, 448–452.
21 P. V. Hauschka and M. L. Reid, *Dev. Biol.*, 1978, **65**, 426–434.
22 B. J. Pollard and G. Kitchen, *Bones and joints*, Elsevier Inc., Sixth Edit., 2017.
23 P. G. Robey, *Connect. Tissue Res.*, 1996, **35**, 131–136.
24 J. E. Ellingsen, *Biomaterials*, 1991, **12**, 593–596.
25 L. C. Palmer, C. J. Newcomb, S. R. Kaltz, E. D. Spoerke and S. I. Stupp, *Chem. Rev.*, 2008, **108**, 4754–4783.
26 V. N. Malashkevich, S. C. Almo and T. L. Dowd, *Biochemistry*, 2013, **52**, 8387–8392.
27 Q. Q. Hoang, F. Sicheri, A. J. Howard and D. S. C. Yang, *Nature*, 2003, **425**, 977–980.
28 R. A. Atkinson, J. S. Evans, P. V. Hauschka, B. A. Levine, R. Meats, J. T. Triffitt, A. S. Virdi and R. J. P. Williams, *Eur. J. Biochem.*, 1995, **232**, 515–521.

29 T. L. Dowd, J. F. Rosen, L. Mints and C. M. Gundberg, *Biochim. Biophys. Acta - Mol. Basis Dis.*, 2001, **1535**, 153–163.

30 C. Andrea, F. Maset, L. De Toni, D. Guidolin, D. Sabbadin, G. Strapazzon, S. Moro, V. De Filippis and C. Foresta, *Front. Biosci.*, 2014, **19**, 1105.

31 P. S. Stayton, G. P. Drobny, W. J. Shaw, J. R. Long and M. Gilbert, *Crit. Rev. Oral Biol. Med.*, 2003, **14**, 370–376.

32 J.-W. Shen, T. Wu, Q. Wang and H.-H. Pan, *Biomaterials*, 2008, **29**, 513–532.

33 J. R. Long, W. J. Shaw, P. S. Stayton and G. P. Drobny, *Biochemistry*, 2001, **40**, 15451–15455.

34 G. K. Hunter, J. O'Young, B. Grohe, M. Karttunen and H. A. Goldberg, *Langmuir*, 2010, **26**, 18639–18646.

35 L. A. Scudeller, S. Srinivasan, A. M. Rossi, P. S. Stayton, G. P. Drobny and D. G. Castner, *Biointerphases*, 2017, **12**, 02D411.

36 V. V. Meretoja, A. E. De Ruijter, T. O. Peltola, J. A. Jansen and T. O. Närhi, *Tissue Eng.*, 2005, **11**, 1489–1497.

37 H. Liu, E. B. Slamovich and T. J. Webster, *Nanotechnology*, 2005, **16**, S601–S608.

38 K. H. Chan, S. Zhuo and M. Ni, *Int. J. Med. Sci.*, 2015, **12**, 701–707.

39 K. G. Sprenger, A. Prakash, G. Drobny and J. Pfaendtner, *Langmuir*, 2018, **34**, 1199–1207.

40 E. Villarreal-Ramirez, R. Garduño-Juarez, A. Gericke and A. Boskey, *Connect. Tissue Res.*, 2014, **55**, 134–137.

41 A. L. Boskey and E. Villarreal-Ramirez, *Matrix Biol.*, 2016, **52**–**54**, 43–59.

42 Z. Xu, Y. Yang, W. Zhao, Z. Wang, W. J. Landis, Q. Cui and N. Sahai, *Biomaterials*, 2015, **39**, 59–66.

43 B. Huang, Y. Lou, T. Li, Z. Lin, S. Sun, Y. Yuan, C. Liu and Y. Gu, *Acta Biomater.*, 2018, **80**, 121–130.

44 A. T. Church, Z. E. Hughes and T. R. Walsh, *RSC Adv.*, 2015, **5**, 67820–67828.

45 J. O'Young, Y. Liao, Y. Xiao, J. Jalkanen, G. Lajoie, M. Karttunen, H. A. Goldberg and G. K. Hunter, *J. Am. Chem. Soc.*, 2011, **133**, 18406–18412.

46 Z. B. Lai, M. Wang, C. Yan and A. Oloyede, *J. Mech. Behav. Biomed. Mater.*, 2014, **36**, 12–20.

47 Z. Xu, Y. Yang, Z. Wang, D. Mkhonto, C. Shang, Z. P. Liu, Q. Cui and N. Sahai, *J. Comput. Chem.*, 2014, **35**, 70–81.

48 W. Zhao, Z. Xu, Q. Cui and N. Sahai, *Langmuir*, 2016, **32**, 7009–7022.

49 T.-J. Lin and H. Heinz, *J. Phys. Chem. C*, 2016, **120**, 4975–4992.

50 T. R. Walsh, *Adv. Exp. Med. Biol.*, 2017, **1030**, 37–50.

51 Q. Xie, Z. Xue, H. Gu, C. Hu, M. Yang, X. Wang and D. Xu, *J. Phys. Chem. C*, 2018, **122**, 6691–6703.

52 X. Wang, L. Zhang, Q. Zeng, G. Jiang and M. Yang, *Appl. Surf. Sci.*, 2018, **452**, 381–388.

53 R. Demichelis, N. A. Garcia, P. Raiteri, R. Innocenti Malini, C. L. Freeman, J. H. Harding and J. D. Gale, *J. Phys. Chem. B*, 2018, **122**, 1471–1483.

54 M. Luo, Y. Gao, S. Yang, X. Quan, D. Sun, K. Liang, J. Li and J. Zhou, *Phys. Chem. Chem. Phys.*, 2019, **21**, 9342–9351.

55 E. L. Buckle, A. Prakash, M. Bonomi, J. Sampath, J. Pfaendtner and G. P. Drobny, *J. Am. Chem. Soc.*, 2019, **141**, 1998–2011.

56 A. A. Skelton, T. Liang and T. R. Walsh, *ACS Appl. Mater. Interfaces*, 2009, **1**, 1482–

1491.
57 S. Monti and T. R. Walsh, *J. Phys. Chem. C*, 2010, **114**, 22197–22206.
58 J. Sampath, A. Kullman, R. Gebhart, G. Drobny and J. Pfaendtner *(under review).*
59 Y. Kang, X. Li, Y. Tu, Q. Wang and H. Ågren, *J. Phys. Chem. C*, 2010, **114**, 14496–14502.
60 M. Předota, A. V. Bandura, P. T. Cummings, J. D. Kubicki, D. J. Wesolowski, A. A. Chialvo and M. L. Machesky, *J. Phys. Chem. B*, 2004, **108**, 12049–12060.
61 M. Deighan and J. Pfaendtner, *Langmuir*, 2013, **29**, 7999–8009.
62 M. Deighan, M. Bonomi and J. Pfaendtner, *J. Chem. Theory Comput.*, 2012, **8**, 2189–2192.
63 M. J. Abraham, T. Murtola, R. Schulz, S. Páll, J. C. Smith, B. Hess and E. Lindahl, *SoftwareX*, 2015, **1**–**2**, 19–25.
64 M. Bonomi, D. Branduardi, G. Bussi, C. Camilloni, D. Provasi, P. Raiteri, D. Donadio, F. Marinelli, F. Pietrucci, R. A. Broglia and M. Parrinello, *Comput. Phys. Commun.*, 2009, **180**, 1961–1972.
65 N. Foloppe and A. D. MacKerell, Jr., *J. Comput. Chem.*, 2000, **21**, 86–104.
66 H. J. C. Berendsen, J. R. Grigera and T. P. Straatsma, *J. Phys. Chem.*, 1987, **91**, 6269–6271.
67 J. L. Desmond, P. M. Rodger and T. R. Walsh, *Mol. Simul.*, 2014, **40**, 912–921.
68 H. Heinz, T.-J. Lin, R. Kishore Mishra and F. S. Emami, *Langmuir*, 2013, **29**, 1754–1765.
69 A. M. Sultan, Z. E. Hughes and T. R. Walsh, *Biointerphases*, 2018, **13**, 06D403.
70 M. D. Hanwell, D. E. Curtis, D. C. Lonie, T. Vandermeersch, E. Zurek and G. R. Hutchison, *J. Cheminform.*, 2012, **4**, 17.
71 B. Hess, H. Bekker, H. J. C. Berendsen and J. G. E. M. Fraaije, *J. Comput. Chem.*, 1997, **18**, 1463–1472.
72 G. Bussi, D. Donadio and M. Parrinello, *J. Chem. Phys.*, 2007, **126**, 014101.
73 M. Parrinello and A. Rahman, *J. Appl. Phys.*, 1981, **52**, 7182–7190.
74 U. Essmann, L. Perera, M. L. Berkowitz, T. Darden, H. Lee and L. G. Pedersen, *J. Chem. Phys.*, 1995, **103**, 8577–8593.
75 G. Bussi, F. L. Gervasio, A. Laio and M. Parrinello, *J. Am. Chem. Soc.*, 2006, **128**, 13435.
76 M. K. Prakash, A. Barducci and M. Parrinello, *J. Chem. Theory Comput.*, 2011, **7**, 2025–2027.
77 A. Barducci, G. Bussi and M. Parrinello, *Phys. Rev. Lett.*, 2008, **100**, 020603.
78 D. J. Earl and M. W. Deem, *Phys. Chem. Chem. Phys.*, 2005, **7**, 3910.
79 K. G. Sprenger and J. Pfaendtner, *Langmuir*, 2016, **32**, 5690–5701.
80 The PLUMED consortium, *Nat. Methods*, 2019, **16**, 670–673.
81 C. M. Mao, J. Sampath, K. G. Sprenger, G. Drobny and J. Pfaendtner, *Langmuir*, 2019, acs.langmuir.8b01392.
82 R. A. Hartvig, M. van de Weert, J. Østergaard, L. Jorgensen and H. Jensen, *Langmuir*, 2011, **27**, 2634–2643.
83 P. V. Hauschka and S. A. Carr, *Biochemistry*, 1982, **21**, 2538–2547.

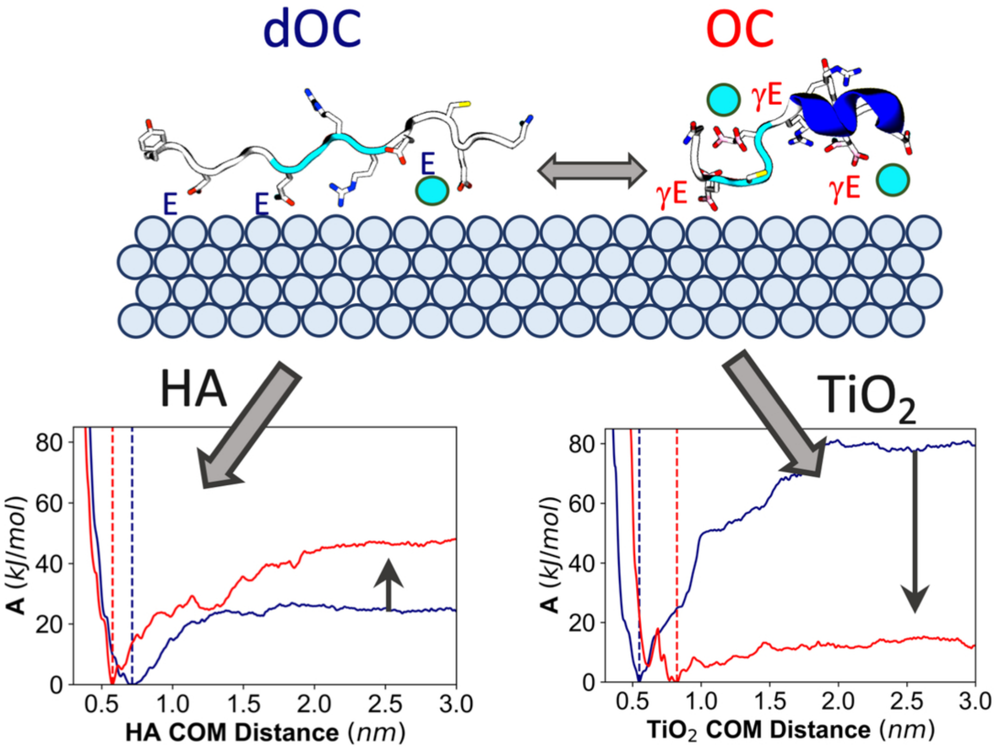

92x69mm (300 x 300 DPI)